DETECTION OF DRAINAGE FAILURE IN RECONSTRUCTED CRANBERRY SOILS USING TIME SERIES ANALYSIS

D. W. Hallema, Y. Périard, J. A. Lafond, S. J. Gumiere, and J. Caron

Laval University
Department of Soils and Agrifood Engineering
Quebec City, Canada

ABSTRACT

A cranberry farm is often a semi-closed water system, where water is applied by means of irrigation and drained using an artificial drainage system. Sufficient drainage early in the season helps to improve rooting depth, which makes crops more resistant to drought and leads to higher cranberry yields. The key to maintaining an optimal water balance is timely irrigation and drainage, and therefore a proper understanding of the interaction between the two is required to increase production efficiency. Current diagnostic methods for identifying drainage failure on cranberry fields are based on outflow from tile drains; however these methods are time-consuming and expensive because the exact locations of tile drains are mostly unknown. In order to reduce the risk of crop disease related to waterlogging and optimize the cranberry production process, we here present an alternative diagnostic approach for detecting drainage failure based on the wavelet transform of hydrological time series obtained with soil column experiments. Wavelet transforms can be used to detect singularities in hydrological time series based on specific criteria, such as wavelet period, frequency, and change in the corresponding wavelet coefficient. Examples demonstrated in this paper are (i) wetting front instability characterized by variations in power response for short wavelets, (ii) long-term drifts that could point to specific characteristics of a laboratory experiment, or in the case of field data, weather conditions, and (iii) drainage failure characterized by a primary component in the CWT power response that shifts toward a longer wavelet period over the course of time.

INTRODUCTION

With an increasing demand for cranberries, the challenge in cranberry production is to improve water productivity and maximize yield by creating optimal conditions in terms of soil water potential (Pelletier *et al.*, 2014). Cranberry farms are essentially semi-closed water systems with artificial sand bogs that are irrigated using a sprinkler system mounted onto conduits buried under the surface, and drained by means of tile drainage. The production process consumes large quantities of water (5000 m^3 ha^{-1} yr^{-1}) for irrigation during the growing season, flooding during harvest and frost protection in winter (Poirier, 2010). Water is drawn from lakes, rivers or streams, and stored in large basins so that it can be recycled for multiple use. While irrigation can be controlled with high precision, drainage failure can develop unnoticed over the course of several years and requires large investments to resolve.

A paper reporting on cranberry cultivation in Wisconsin in 1853 mentions the use of ditches to drain excess water from bogs and flooding when the ground has become too dry (Durand, 1942). Flooding is no longer necessary for this purpose with the arrival of modern irrigation systems, however cranberry bogs must be drained to the water level inside the surrounding ditches in order to maintain an optimal pore pressure within the root zone. This is important for a number of reasons. First of all, *Phytophthara* causing root rot are commonly associated with irrigation with contaminated surface water (Oudemans, 1999) and enhanced by waterlogging in the root zone (Roberts *et al.*, 2005). Secondly, a deeper rooting depth increases the cranberry's chances of survival during periods of drought. Sufficient drainage early in the season helps to improve rooting depth (Sandler *et al.*, 2004) because the vines extend their root network toward deeper soil layers where flushed nutrients accumulate. For these reasons growers report a generally better yield on bogs with tile drainage where excess soil water is removed through gravity-driven flow.

Timely irrigation and drainage are essential, and therefore a proper understanding of the relationship between irrigation and drainage is necessary to increase the production efficiency of cranberry farms. Current diagnostic tools for detecting drainage failure are mostly based on outflow from tile drains: when outflow decreases after a number of years as a result of clogging, drains are either cleaned or replaced. These methods are time-consuming and expensive because it is often necessary to excavate in order to find the tile drains.

We here present an alternative diagnostic approach for drainage failure detection based on the wavelet transform of hydrological time series obtained with soil column experiments. In the first part of the paper we illustrate the basics of the wavelet analysis by presenting the discrete wavelet transform of two Dohono and Johnstone (1994) test functions, and in the second part of the paper we discuss the more accurate continuous wavelet transform of time series of tensiometer data from a soil column experiment (Périard *et al.*, 2014).

Functional transforms and hydrological time series analysis

Functional transforms can be used to convert a given function into another function, or into a series of functions. The Fourier transform can decompose a given signal $f(t)$ into a series of complex sinusoids $e^{j\omega t}$ and is given by:

$$F(j\omega) = \int_{-\infty}^{\infty} f(t)e^{-j\omega t}dt \tag{1}$$

where $F(j\omega)$ represents the amplitudes of the family of sinusoidal base functions $e^{j\omega t}$. Fourier transforms are often used in digital signal processing to speed up algorithms, because all operations in the time domain have an equivalent in the frequency domain that is often faster depending on the complexity of the signal. However, the main drawback of the Fourier transform is that the non-stationary transient information on the phase of the signal is lost after transformation, which makes it impossible to determine the timing of a particular singularity, *e.g.* drainage failure in a hydrological time series. To resolve this, a windowing technique can be used in which the Fourier transform is applied to a short time frame that allows the estimation of the timing of an event, however the precision of the timing is limited to the window length. Likewise, the exact phase of the signal can only be determined by approximation because the frequency resolution of the window is inversely proportional to the window length according to the Heisenberg uncertainty principle.

Contrary to the Fourier transform, where the base functions are sinusoids that are frequency-localized but not time-localized because they extend from -∞ to +∞, the wavelet transform can decompose a time series into a series of functions that are localized in both frequency and time. The wavelet transform uses different window sizes adapted to the analyzed frequency and time period of the signal at the same time, whereas a Fourier transform uses a fixed-size window of frequencies only. For this reason, the wavelet transform is more flexible and efficient for time series analysis than the Fourier transform, and nowadays applications are found in many bogs, including data compression, earthquake prediction and climate analysis (Burrus *et al.*, 1998).

The wavelet transform can also be applied to data sequences, which is very useful for filtering known signals from a time series of observations and identifying time trends. Applications include the spatial decomposition of rainfall data into large- and small-scale rainfall patterns (Kumar and Foufoula-Georgiou, 1993), analysis of variability in annual stream flow (Coulibaly and Burn, 2004), detection of long-term trends in stream flow data (Adamowski *et al.*, 2009), and stream flow forecasting (Anctil and Tape, 2004). An overview of applications in hydrological time series analysis can be found in Sang (2013). Within the context of time series analysis, wavelet transforms have been used for tool monitoring in milling operations (Lee and Tarng, 1999), where tool failure was detected using a four-level wavelet decomposition of a spindle motor current signal. An irregular drainage pattern can be detected in the same way as a tool failure: such pattern deviates from patterns expected based on the design drainage in response to rainfall, irrigation, and evapotranspiration.

DISCRETE WAVELET TRANSFORM FOR MULTI-SCALE TIME SERIES ANALYSIS

Theory (Nason, 2008; Dohono and Johnstone, 1994)

The multi-scale discrete wavelet transform (DWT; Haar, 1910; Mallat, 1989) employs a scaling coefficient to translate a time series into a series of wavelets. The transformation is performed on a vector of size $n = 2^J$ that is obtained by appending *n-N* zeros to a time series of arbitrary length *N*, and involves the calculation of detail and smoothed coefficients for time series vector y at progressively coarse scales.

The detail coefficient at the finest time scale is defined as the difference between successive pairs of observations:

$$d_k = y_{2k} - y_{2k-1} \tag{2}$$

where k is the localized time index with $k = 1, \ldots, n/2$. The resulting sequence $\{d_k\}_{k=1}^{n/2}$ is the local difference vector of non-overlapping pairs with $d_1 = y_2 - y_1$, $d_2 = y_4 - y_3$, $d_3 = y_6 - y_5$, etc. Next, the smoothed coefficient at the finest time scale is given by the scaled local averages of successive pairs of observations, formulated as:

$$c_k = y_{2k} + y_{2k-1} \tag{3}$$

for $k = 1, \ldots, n/2$. The scaled local average vector $\{c_k\}_{k=1}^{n/2}$ is appropriately so named because we add non-overlapping pairs of adjacent observations in vector y without dividing by n. c_k can therefore be viewed as a scaled moving average that is similar to a smoothing coefficient.

Detail coefficient d_k and smoothed coefficient c_k are determined for progressively coarser levels of detail (or resolution) of y, indicated by subscript j. We can now write d_k as $d_{J-1,k}$ given that the finest level of detail corresponds with $j = J - 1$ observations. For the next coarsest level of detail (level 2) we calculate the detail coefficient as:

$$d_{J-2,\ell} = c_{J-1,2\ell} - c_{J-1,2\ell-1} = (y_{4\ell} + y_{4\ell-1}) - (y_{4\ell-2} + y_{4\ell-3}) \tag{4}$$

for $\ell = 1, \ldots, n/4$. The smoothing coefficient for level 2 becomes:

$$c_{J-2,\ell} = c_{J-1,2\ell} + c_{J-1,2\ell-1} = (y_{4\ell} + y_{4\ell-1}) + (y_{4\ell-2} + y_{4\ell-3}) \tag{5}$$

The detail and smoothing coefficients are more commonly known as the wavelet and scale coefficients. Each wavelet and scale corresponds with a resolution level. The number of coefficients reduces by a factor 2 for each successive level, until there is only one coefficient left (for *j=0*).

The efficiency of the DWT becomes clear when we consider the sparsity of the wavelet coefficients. Vectors with unchanging data values result in wavelet

coefficients that are zero for multiple scales, until a different value is encountered. This means that piecewise smooth vectors have sparse wavelet representations.

The discrete wavelet and scaling function coefficients are finally normalized by applying filters to the wavelet coefficients calculated for each scale to ensure that the norm, or energy, of the output sequence equals the norm of the input sequence. The energy of the input sequence is given by $\|y\|^2$ and the energy of the output sequence is given by $\|d_k\|^2$ so that:

$$d_k = \sum_{\ell=-\infty}^{\infty} g_\ell y_{2k-\ell} \tag{6}$$

where

$$g_\ell = \begin{cases} -2^{-1/2} & for\ \ell = 0, \\ 2^{-1/2} & for\ \ell = 1, \\ 0 & otherwise \end{cases} \tag{7}$$

The Haar wavelet transform is now given by the sum of a wavelet function (ϕ), also referred to as the kernel function or mother wavelet, and the set of detail representations (ψ) for all resolution levels:

$$f(y) = \sum_{k\in\mathbb{Z}} c_{j_0,k} \phi_{j_0,k}(y) + \sum_{j=j_0}^{\infty} \sum_{k\in\mathbb{Z}} d_{j,k} \psi_{j,k}(y) \tag{8}$$

Analysis of hypothetical time series with the DWT

In order to demonstrate the advantage of the DWT in time series analysis we generated and transformed two hypothetical time series with the Wavethresh software package written for R (Nason, 2008). The first time series represents the Doppler effect, starting with a high frequency that gradually decreases over time (Figure 1a). It was generated using the following test function (Dohono and Johnstone, 1994):

$$f(t) = \{t(1-t)\}^{\frac{1}{2}} \sin\{2\pi(1+\varepsilon)/(t+\varepsilon)\} + Z(t), \quad \varepsilon = 0.05 \tag{9}$$

where t is time and $Z(t)$ defines a random time function (or white noise model) with zero mean and a signal to noise ratio of 15 to 1. The random time function was added to emulate a sensor signal with unexplained variance. After decomposing the time series vector with a total length of $n = 1024$ samples we obtain $\log_2(1024) = 10$ resolution levels that are numbered 0 to 9 in Figure 1a corresponding with the coarsest and finest level of detail, respectively. The wavelet coefficients plotted for level 9 that show the high-frequency component with a period $T=1$ reach a maximum after time $t=13$. Subsequently, the amplitude slowly decays until no more time-dependent structure can be detected as it blends with the white noise (after approximately $t=512$, which has an equivalence of 256 in the wavelet basis function's translate number in the graph on the right hand side of Figure 1a). The timing of events for resolution level 9 can be established with a small error of $T=2$ (calculated as $n \times 2^{-9}$), however the timing of events becomes increasingly inaccurate for lower resolution levels. The level 5 wavelet maximum is reached after $t=144$, determined with an error of $t=32$ (calculated as $n \times 2^{-5}$),

while the timing of the level 0 maximum after t=512 has an error as high as t=1024 ($n \times 2^0$). Apparently the time series is not long enough to be able to estimate the timing of this type of low-frequency components.

Despite a negative relationship between wavelet period and timing error, the DWT method is very useful for detecting singularities in the high frequency domain. Figure 1b shows a second time series defined by the following test function (Dohono and Johnstone, 1994):

$$f(t) = 4\sin 4\pi t - sgn(t - 0.3) - sgn(0.72 - t) \tag{10}$$

where the signum function is defined as:

$$sgn(t) = \begin{cases} -1 & if\ t < 0 \\ 0 & if\ t = 0 \\ 1 & if\ t > 0 \end{cases} \tag{11}$$

After a discrete wavelet transform, event can be detected in the transformed wavelets based on specific criteria, such as wavelet period, frequency and the change in the corresponding wavelet coefficient. This change is evaluated for the mother wavelet containing the differences between successive pairs of observations (wavelet coefficients) calculated for a resolution level. The time series in Figure 1b has two jumps that were detected by filtering the wavelets with period T=2 (resolution level 8) and a wavelet coefficient threshold of 0.2 absolute.
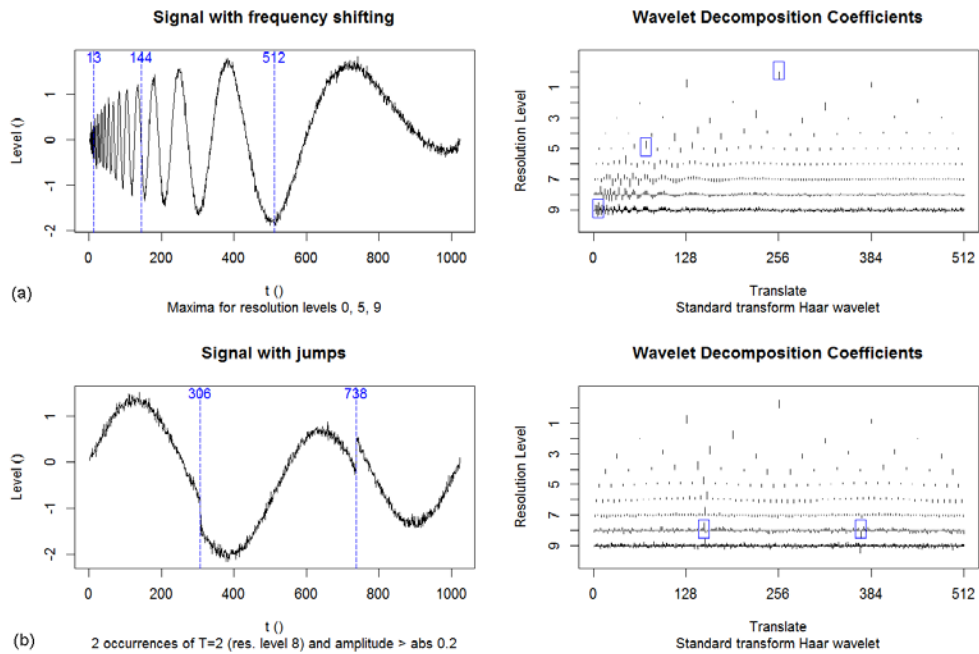
Figure 1. Discrete wavelet transform and event detection for Dohono and Johnson test functions with a 15:1 signal to noise ratio (examples found in Nason, 2008).

CONTINUOUS WAVELET TRANSFORM FOR THE COMPLETE TIME-SCALE ANALYSIS OF TIME SERIES DATA

Theory (Farge, 1992; Torrence and Compo, 1998)

While the multi-scale DWT can be used to detect events in the high-frequency domain, it is not very accurate for the low end of the frequency domain because the discrete wavelet uses only a subset of wavelet coefficients to decompose a time series. A complete time-scale representation of local and transient events associated with different frequencies can be obtained with a continuous wavelet transform (CWT; Farge, 1992), and this transform allows for a higher accuracy in determining the timing of these events.

The continuous wavelet transform of time series vector y is defined as the convolution of y_j with a scaled and translated version of wavelet function ψ_0:

$$W_m(s) = \sum_{m'=0}^{N-1} y_{m'} \psi^* \left[\frac{(m'-m)\delta t}{s} \right] \tag{12}$$

where an overview is obtained of how amplitudes of detail representations (given by the complex conjugate ψ^*) of the original time series (y) are scaled and translated along the continuous wavelet scale (s) and discrete localized time index (m). The continuous wavelet scale is the equivalent of the resolution level in the DWT. In order to qualify as a wavelet function, ψ_0 must be localized in both time and frequency space and have zero mean (Farge, 1992). Here we used the Morlet wavelet, a complex non-orthogonal plane wave (*i.e.* a wave whose maxima are equally spaced) modulated by a Gaussian function:

$$\psi_0(\eta) = \pi^{-0.25} e^{i\omega_0 \eta} e^{-0.5\eta^2} \tag{13}$$

where ω_0 is a nondimensional frequency, and η a non-dimensional time parameter. Here we used $\omega_0=6$ to satisfy the zero mean condition.

A wavelet power spectrum facilitates the analysis of the CWT, and is obtained by normalizing the absolute expectation value of $W_m(s)$ with respect to the average variance σ^2 over a range of scales:

$$|W_m(s)|^2 / \sigma^2 \tag{14}$$

The longest period for which observed trends can be detected depends on the length of the time series. A study on the variability in annual Canadian stream flows assumes that their 88-year dataset can be used to detect variance for periods up to 12 years, or 7 complete cycles in the time series (Coulibaly and Burn, 2004).

(a)	**(b)**
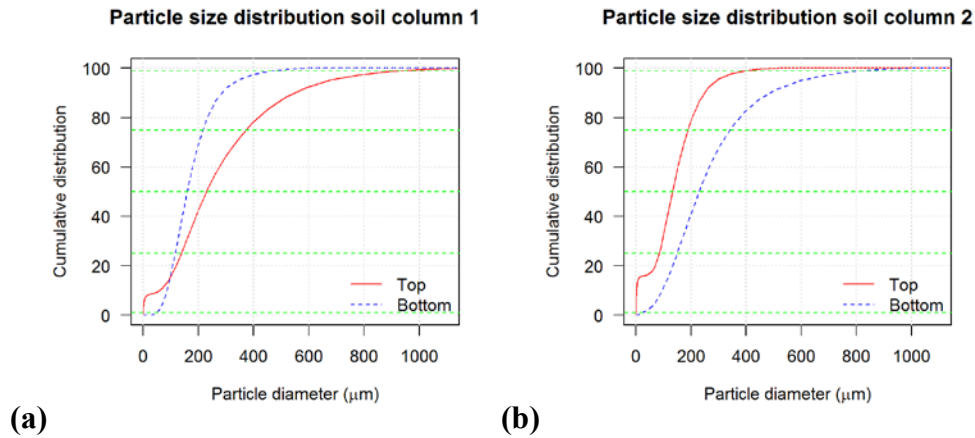
Figure 2. Cumulative particle size distributions at depths of 10-15 cm (denoted "Top") and 71-85 cm (denoted "Bottom") for the two soil columns after the experiment.

Experimental time series of tensiometer data

An experiment was designed to simulate the effects of variations in the groundwater level on the hydrodynamic response of the sandy substrate of cranberry bogs (Périard *et al.*, 2014). Two sandy soils typically found on cranberry bogs were reconstructed in a laboratory setting using transparent columns with a height of 100 cm and a diameter of 15.24 cm (6 inches). The base material was added in layers of 2 cm and spread out every time to obtain a uniform bulk density of 1.6 g.cm^{-3}. Material of the upper 20 cm was mixed with 5 g of zirconium oxide (ZrO_2) tracer per 100 g of sand. This tracer exists of spherical particles with d_{50}=1.25 μm, which corresponds to the size of colloidal particles, and is considered inert for the purpose of this study. The composition of the soil columns after the experiment is plotted in Figure 2 and can be summarized as follows:

- Soil column 1: 20 cm of medium coarse sand (median particle size d_{50}=229 μm) on top of 80 cm of fine sand (d_{50}= 174 μm);
- Soil column 2: 20 cm of fine sand (d_{50}=133 μm) on top of 80 cm of medium coarse sand (d_{50}=229 μm).

Both columns were placed in the experimental setup shown in the schematic of Figure 3. Three components controlled the flow inside the column and were activated by opening or closing the valves.

- Recharge component: Recharge was activated by the control unit (Campbell CR-10) by opening an acting valve (A) and closing a second acting valve (B; Asco 8262), following which a constant head of 76 cm was applied to the bottom of the column. The constant head was established using a Mariotte's bottle that maintained atmospheric pressure at 76 cm above the bottom of the soil column by letting air enter at that level.
- Drainage component: Drainage occurred when the control unit closed valve A and opened valve B (reversed valve position with respect to the

recharge mode), in which case a 5 cm suction was applied by an Erlenmeyer flask with a water inlet 5 cm below the bottom of the soil column.

- Irrigation component: By opening valve C a constant head of 9 cm was applied equally across the top surface of the soil column. Again a Mariotte's bottle was used to establish the constant head.

PX-26 tensiometers were placed at depths of 5, 15, 25, 35, 45, 55, 65, 75, 85 and 95 cm in order to monitor the pressure over time. The experiment was started by saturating the soil columns to a depth of 35 cm below the top, after which the columns were allowed to drain to a depth of 55 cm under a suction of 5 cm applied to the bottom. The control unit was programmed to alternately activate the recharge and drainage modes in the following loop sequence:

- Recharge mode was activated as soon as the pressure of the tensiometer installed at a depth of 55 cm dropped below zero, meaning that the groundwater level reached a depth of 55 cm. Recharge mode caused an upward flux of water inside the column resulting from a 76 cm constant head applied to the bottom of the column.
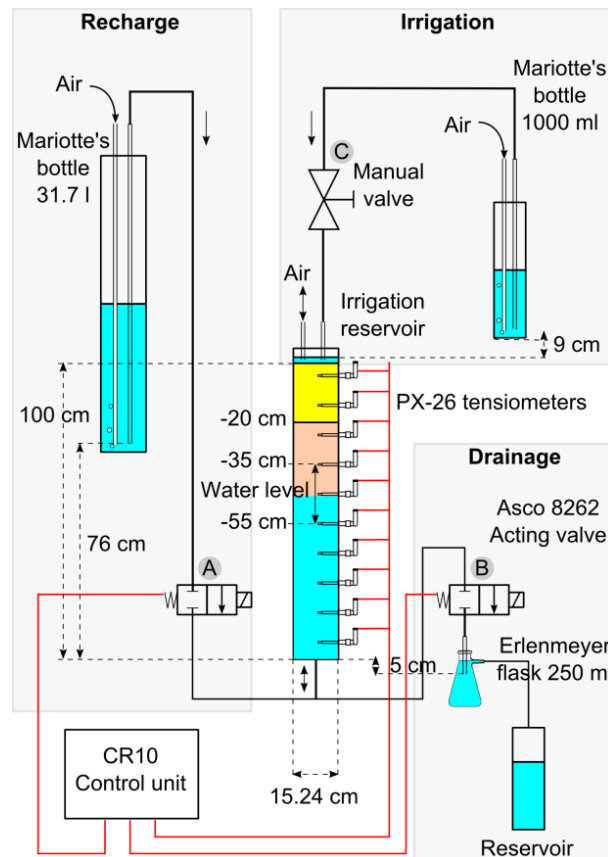
Figure 3. Schematic of the soil column experiment. After saturating the soil column from the bottom up to 35 cm below the top, the water level oscillated between –55 cm and –35 cm by alternately opening the recharge valve (A) and drainage valve (B). Irrigation was initiated by opening valve C.

- Drainage mode was activated as soon as the pressure of the tensiometer at a depth of 35 cm exceeded zero, meaning that the groundwater level reached the level of this tensiometer. In this mode, the soil was allowed to drain by means of downward gravitational flow and a suction of 5 cm.

The irrigation mode was activated once during the entire sequence independently from the recharge and drainage modes.

### Analysis of experimental time series with the CWT

Figure 4 shows the pressure time series and the normalized wavelet power spectra obtained after a continuous wavelet transform of data for the top and bottom sensors in soil column 1 with 20 cm of medium coarse sand on top of 80 cm of fine sand. The top and bottom sensors correspond with a depth of 5 cm below the surface (within the top layer of fine sand), and for the bottom sensor at a depth of 85 cm (within the bottom layer). CWTs were performed using the dplR package written for R (Bunn, 2008). Taking the pressure time series with one-minute sampling intervals as input, we calculated the CWTs between scales 0 and $2^{10} = 1024$ so that the maximum possible period of the transformed wavelets was 1024 minutes (17 hours). This is the range of the vertical axis in the contour plots of the CWTs, and within this range four sub-octaves were calculated per octave (four scales per power of two) yielding a total of $4 \times 2^{10} = 4096$ scales. Colors vary between yellow (low power response) and blue to violet (high power response), while grey shades represent random noise for which $|W_m(s)|^2 < \sigma^2$. A cone of influence was also added to the plot to indicate the region of interest, given that the diagonally hatched areas at the beginning and end of the time series mark the range where the CWT is influenced by boundary effects.

The top sensor of soil column 1 recorded a pressure oscillating between –43.4 cm and –30.4 cm (Figure 4a), corresponding with the alternating opening and closing sequence of the recharge and drainage valves. For the bottom sensor we observed pressure oscillations between 22.6 cm and 51.5 cm, meaning the water level stood between the top and bottom sensors at all times during the experiment (Figure 4b). At $t=1018$ min, 60 mm of irrigation was applied with a Mariotte's bottle that maintained a constant head of 9 cm at the soil surface for a duration of 50 min. This irrigation event was detected by both sensors, and is visible in the CWT power spectrum (Figure 4a and b) as a cone-shaped blue zone centered on $t=1036$ min. The wavelet with period $T=5$ min at $t=1018$ min (represented by a green zone in the CWT of Figure 4a) marks the onset of the irrigation event, after which the uniform spatial and temporal distribution of irrigation causes a very abrupt power response maximum for wavelets with a period longer than $T=1$ hour for the top sensor at a depth of 5 cm below the surface.

Now the recharge-drainage cycle contains two dominant wavelets, which are most visible in the CWT after $t=2500$ min. There we observe two blue bands, the upper wider than the lower, that can be followed diagonally across the CWT and that extend across the entire time series. The wide band corresponds to the process with the longest wavelet periods, *i.e.* recharge, while the narrow band corresponds to the process with a series of shorter wavelet periods, *i.e.* drainage. Recharge starts with a wavelet period of $T=40$ min at $t=50$, and slows down to approximately $T=6$ hours at $t=3000$ min, which is after 29 recharge-drainage

cycles. Similarly, drainage starts with a wavelet period of T=20 min at t=50 min, and decreases to T=3 hours at t=3000 min. Hence, the drainage is approximately two times faster than recharge. A quick calculation learns that the duration of the recharge-drainage cycle increases on average by 7.9% per cycle throughout the time series, which is evidence of severe drainage failure almost immediately after the beginning of the experiment.

While the top sensor wavelets with a short period (lower boundary of the CWT in Figure 4a) follow a stable pattern in the beginning, they become increasingly irregular after the irrigation event (t=1060 min) and are characterized by a greater amount of white noise distributed over a wide range of scales in the

(a)

(b)
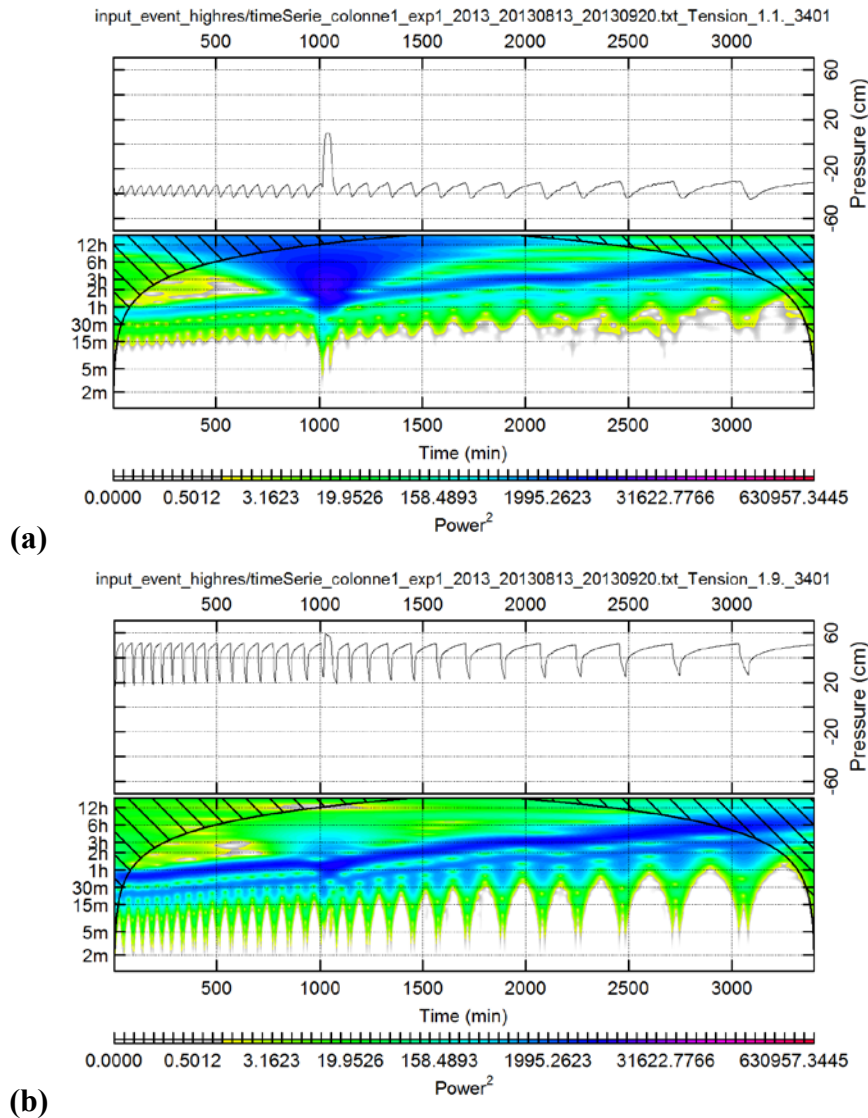
Figure 4. Pressure time series and CWT for soil column 1, which contains a profile with 20 cm of medium coarse sand on top of 80 cm of fine sand. Pressure for the top sensor at 5 cm (a) and the bottom sensor at 85 cm (b) below the surface. Diagonally hatched areas at the beginning and end of the sequence mark the range where the CWT is influenced by boundary effects.

high end of the frequency domain (plotted in grey shades in Figure 4a). This phenomenon is most likely explained by the timing of irrigation, which is started in drainage mode while a 5 cm suction is applied at the bottom of soil column 1. The suction creates an air pressure potential in the partially saturated upper part of the column and causes the air to redistribute within the profile. As a result, the wetting front becomes instable and the top sensor detects short-term variations in pressure that remain nearly undetected by the bottom sensor (Figure 4b).

At a more detailed level we can observe that the pressure time series follow a concave downward pattern during the recharge periods. For the bottom sensor we furthermore observe that the drainage periods are characterized by a concave

(a)

(b)
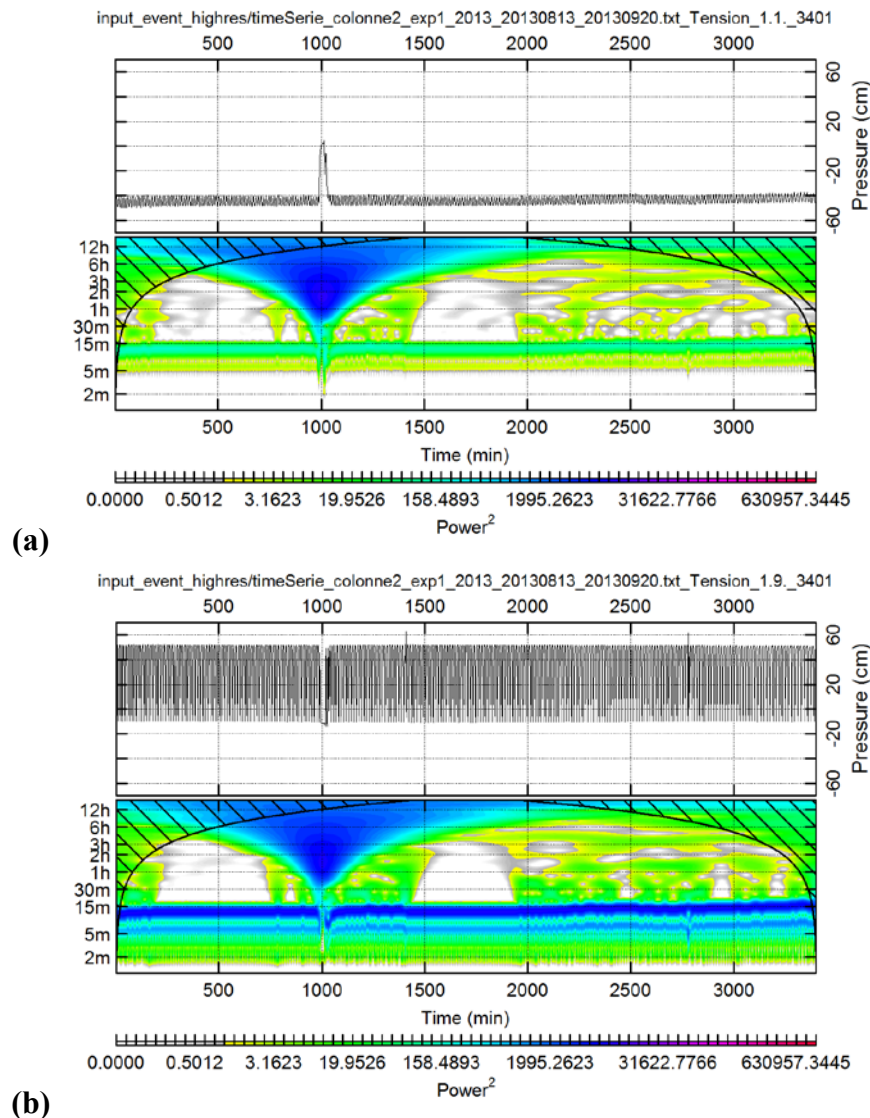
Figure 5. Pressure time series and CWT for soil column 2, which contains a profile with 20 cm of fine sand on top of 80 cm of medium coarse sand. Pressure for the top sensor at 5 cm (a) and the bottom sensor at 85 cm (b) below the surface.

upward pattern, which is reflected by a periodically decreasing period of the secondary component (the lower narrow dark blue band in Figure 4b with conical shapes suspended from the bottom).

The reversed soil layer sequence in column 2, which contains a profile with 20 cm of fine sand on top of 80 cm of medium coarse sand, leads to a rather different response with only a very slight increase of the drainage wavelet period from T=7 min at t=50 min to T=9 min at t=3000 min (lower horizontal green band in Figure 5a and lower horizontal blue band in Figure 5b). With a total of 264 recharge-drainage cycles the increase in period is 0.1% on average per cycle, still not negligible in the long run but nevertheless much lower than the 7.9% increase per cycle observed for the medium coarse on fine sand profile of soil column 1. Again we observe a concave downward pattern for the pressure curve during the recharge periods and a concave upward pattern during the drainage periods.

The wetting front after irrigation is not as unstable as in soil column 1, however a second phenomenon observed in the CWT of soil column 2 data is that the sensor signal develops a slight drift after t=2000 min with a period between T=30 min and T=6 hours, which could point to the need to recalibrate the sensors.

CONCLUSION

Wavelet transforms can be used to detect singularities in hydrological time series based on specific criteria, such as wavelet period, frequency, and change in the corresponding wavelet coefficient. Examples demonstrated in this paper are (i) wetting front instability characterized by variations in power response for short wavelets, (ii) long-term drifts that could point to specific characteristics of a laboratory experiment, or in the case of field data, weather conditions, and (iii) drainage failure characterized by a primary component in the CWT power response that shifts toward a longer wavelet period over the course of time.

The recharge-drainage cycle in soil column 2 remained relatively constant, while column 1 showed evidence of serious drainage failure in combination with an unstable wetting front. In a future study we want to link these outcomes to the texture distribution and spatio-temporal distribution of the zirconium oxide tracer in the soil columns, in order to be able to propose an optimal irrigation and drainage design for cranberry farms. Such an approach would involve measurement of physical and hydraulic characteristics of soil samples and computational modeling of the hydraulic processes in the soil in response to soil texture and water retention characteristics.

REFERENCES

Adamowski, K., Prokoph, A., and Adamowski, J., 2009. Development of a new method of wavelet aided trend detection and estimation. Hydrological Processes 23: 2686-2696.

Anctil, F., and Tape, D. G., 2004. An exploration of artificial neural network rainfall-runoff forecasting combined with wavelet decomposition. Journal of

Environmental Engineering and Science, 2004, 3(S1): S121-S128, 10.1139/s03-071

Bunn, A. G., 2008. A dendrochronology program library in R (dplR). Dendrochronologia 26(2): 115-124.

Burrus, C. S., Gopinath, R. A., Guo, H., 1998. Introduction to wavelets and wavelet transforms: A primer. Upper Saddle River, NJ, Prentice Hall.

Coulibaly, P., and Burn, D. H., 2004. Wavelet analysis of variability in annual Canadian streamflows. Water Resources Research 40: W03105.

Dohono, D. L., and Johnstone, I. M., 1994. Ideal spatial adaptation by wavelet shrinkage. Biometrika 81(3): 425-455.

Durand, L. Jr., 1942. Wisconsin cranberry industry. Economic Geography 18(2): 159-172.

Farge, M., 1992: Wavelet transforms and their applications to turbulence. Annu. Rev. Fluid Mech., 24, 395–457.

Haar, A., 1910. Zur Theorie der orthogonalen Funktionensysteme. Mathematische Annalen 69: 331-371.

Kumar, P., and Foufoula-Georgiou, E., 1993. A multicomponent decomposition of spatial rainfall fields 1. Segregation of large- and small-scale features using wavelet transforms. Water Resources Research 29(8): 2515-2532.

Lee, B. Y., and Tarng, Y. S., 1999. Application of the discrete wavelet transform to the monitoring of tool failure in end milling using the spindle motor current. International Journal of Advanced Manufacturing Technology 15: 238-243.

Mallat, S. G., 1989. A theory for multiresolution signal decomposition: the wavelet representation. IEEE Transactions on Pattern Analysis and Machine Intelligence 2(7): 674-693.

Nason, G.P., 2008. Wavelet methods in Statistics with R. Springer, New York.

Oudemans, P. V., 1999. Phytophthora Species Associated with Cranberry Root Rot and Surface Irrigation Water in New Jersey. Plant Disease 83 (3): 251-258. DOI: 10.1094/PDIS.1999.83.3.251

Pelletier, V., Gallichand, J., and Caron, J., 2013. Effect of soil water potential threshold for irrigation on cranberry yield and water productivity. Transactions of the ASABE, 56(6): 1325-1332.

Périard, Y., Gumiere, S. J., Rousseau, A. N., Caron, J., and Hallema, D. W., 2014. Impact of anthropomorphic soil genesis on hydraulic properties: the case of cranberry production. Vol. 16, EGU.

Poirier, I., 2010. La canneberge au Québec et dans le Centre-du-Québec - Un modèle de développement durable, à la conquête de nouveaux marchés. In: d. P. e. d. l. A. Ministère de l'Agriculture and Direction régionale du Centre-du-Québec, editors. 2014-8120.

Roberts, P. D., Urs, R. R., French-Monar, R. D., Hoffine, M. S., Seijo, T. E. and McGovern, R. J., 2005. Survival and recovery of Phytophthora capsici and oomycetes in tailwater and soil from vegetable fields in Florida. Annals of Applied Biology 146: 351–359. doi: 10.1111/j.1744-7348.2005.040120.x

Sandler, H. A., DeMoranville, C. J., Lampinen, B., 2004. Cranberry irrigation management. Cranberry station Fact Sheet. Paper 12.

Sang, Y. F., 2013. A review on the applications of wavelet transform in hydrology time series analysis. Atmospheric Research 122: 8-15.

Torrence, C., and Compo, G. P., 1998. A practical guide to wavelet analysis. Bulletin of the American Meteorological Society 79(1): 61-78.